Real time 3D imaging of microstructure growth in battery cells using indirect MRI

Andrew J. Ilott,[a] Mohaddese Mohammadi,[a] Hee Jung Chang,[b] Clare P. Grey,[b,c] and Alexej Jerschow[a,1]

[a]Department of Chemistry, New York University, 100 Washington Square East, New York, New York 10003, USA.
[b]Department of Chemistry, Stony Brook University, Stony Brook, New York 11794-3400, USA.
[c]Department of Chemistry, University of Cambridge, Lensfield Road, Cambridge CB2 1EW, UK.
1. To whom correspondence should be addressed. Email: alexej.jerschow@nyu.edu. Telephone: +1 212 9988451.

Short Title (50 characters): Real time 3D imaging of dendrite growth in batteries

Classification: PHYSICAL SCIENCES: Chemistry

Keywords: Li-ion batteries | in situ MRI | dendrite growth

Abstract

Lithium metal is a promising anode material for Li-ion batteries due to its high theoretical specific capacity and low potential. The growth of dendrites is a major barrier to the development of high capacity, rechargeable Li-ion batteries with lithium metal anodes, and hence significant efforts are undertaken to develop new electrolytes and separator materials that can prevent this process or promote smooth deposits at the anode. Central to these goals, and to the task of understanding the conditions that initiate and propagate dendrite growth, is the development of analytical and non-destructive techniques that can be applied *in situ* to functioning batteries. Magnetic Resonance Imaging (MRI) has recently been demonstrated to provide non-invasive imaging methodology that can detect and localize microstructure buildup. However, until now monitoring dendrite growth by MRI has been limited to observing the insensitive metal nucleus directly, thus restricting the temporal and spatial resolution, and requiring special hardware and acquisition modes. We present here an alternative approach to detect a broad class of metallic dendrite growth via their indirect effects on the surrounding electrolyte, allowing for the application of fast 3D ^{1}H MRI experiments with high resolution. We use these experiments to reconstruct 3D images of growing Li dendrites from MRI, revealing details about the growth rate and fractal behavior. Radiofrequency and static magnetic field calculations are used alongside the images to quantify the amount of the growing structures.

Significance Statement

Lithium metal is an ideal anode material for rechargeable Li-ion batteries but its use is prevented by the growth of lithium deposits, or “dendrites”, during charging that can cause performance loss and serious safety concerns. Understanding the growth of dendrites *in situ* is crucial for the progress of this technology. MRI has been limited to directly studying the lithium signal until now, resulting in low sensitivity, limited resolution, and long experiment times. We present here an approach that detects the ‘shadows’ of dendrites growing through the electrolyte, allowing their growth to be imaged very quickly in 3D with high resolution. This technique can also be applied to other electrodes, such as those based on sodium and magnesium.

Lithium metal is a promising anode material for secondary lithium batteries because it has the highest theoretical specific capacity of possible anode materials (3860 mA h g^{-1}), and the lowest voltage. Its use is currently limited due to irregular microstructure buildup on the electrode during charging (1). These mossy, needle-like, or dendritic structures severely compromise battery performance and can eventually penetrate the separator and cause overheating and short circuiting, thus presenting serious safety concerns. Preventing dendrite growth has proven to be extremely challenging, due in part to current poor understanding of the conditions under which their growth is initiated and the factors that contribute to their continued growth (2, 3). The development of new analytical techniques that are sensitive to dendrite growth and amenable to studying electrochemical cells *in situ* is crucial to future efforts of improving battery designs and performance (4, 5).

In situ nuclear magnetic resonance (NMR) spectroscopy and magnetic resonance imaging (MRI) are powerful non-invasive methods that can provide time-resolved and quantitative information about the changes within the electrolyte and the electrodes. NMR measurements are sensitive to dendrite growth, and are also able to resolve different lithium microstructure morphologies through chemical shift measurements (6–9). MRI approaches provide additional spatial information, allowing specific structural changes to be localized, thereby enhancing the utility of the methods and simplifying interpretation (7, 10, 11). Previous work relied on the measurement of ^{7}Li and ^{6}Li signals, where the identification of dendrites could be achieved via changes in the intensities and frequencies of the Li-metal signals due to skin-depth effects, and susceptibility shifts, respectively (6–10, 12). The main limitations of resolution and imaging time arise from the inherent insensitivity of the lithium isotopes and relaxation phenomena.

Here we demonstrate a new approach; rather than imaging dendrites directly, their interactions with the electrolyte can be used to measure their growth indirectly. Three effects are considered: [1] the displaced volume in the electrolyte, [2] the magnetic susceptibility effects on the electrolyte, and [3] the radio-frequency (rf) field effects on the electrolyte signal. The electrolyte is typically composed of proton-rich material (e.g. LP30, which is composed of 1M $LiPF_6$ in 1:1 ethylene carbonate:dimethyl carbonate), thereby providing excellent sensitivity for measurements of ^{1}H spins. As a result, full three-dimensional measurements become possible that track dendrite growth as a function of time.

Results and Discussion

Figure 1 shows a time series of 3D images of dendrite growth together with the symmetrical Li metal electrode cell geometry. The images, acquired using ^{1}H FLASH imaging performed *in situ* on the electrochemical cell (Figure 1a), show there to be a relatively uniform intensity in the electrolyte region initially, with dark regions extending from *z* = 4 and -4 mm corresponding to the two Li electrodes. The first image (Figure 1a, left) shows the starting configuration of the cell after dendrite growth had been initiated by charging at 50 μA (0.16 mA cm^{-2}) for 72 hours (total charge applied, $Q_{\mathrm{tot}} = 13.0$ Coulombs) (7). As further current is passed (referred to here as "charging" since this is the direction of current flow in a full cell when Li plating occurs) (Figure 1a, left to right), a feature grows out from the left side of the top electrode into the middle of the electrolyte region, and spans the full electrolyte cavity to reach the bottom electrode by *t* = 26.1 hours ($Q_{\mathrm{tot}} = 28.0$ Coulombs). The morphology and progressive "growth" of this feature between the electrodes is indicative of a dendritic microstructure.

Segmenting the images into regions above and below a threshold intensity, $I_{\mathrm{threshold}} = 0.2I_{\mathrm{max}}$ (Figure 1b), emphasizes the position and growth of the microstructure. $I_{\mathrm{threshold}}$ was chosen to provide good image contrast while maintaining the 3D structure of the reconstructed dendrite. Factors affecting the choice of $I_{\mathrm{threshold}}$ are discussed in more detail below. A movie showing the full time series of images collected every 17 mins during a 26.1 hr charge is supplied as supplementary material, along with a movie illustrating the reconstructed dendrite geometry from the final MRI image (same data as Figure 1c, right).

This methodology offers considerable advantages over 3D imaging techniques observing ^{7}Li metal, which require larger scan times (13). Our current approach offers 180 μm isotropic resolution within 16 min 40 s scans, with potential for further optimization due to the increased signal-to-noise ratio and favorable MR properties of the ^{1}H nucleus, and the contrast enhancement afforded by the long-range susceptibility effects. The ability to observe microstructural lithium growth *in situ* and in 3D provides a unique opportunity to study the mechanisms underlying these processes. For example, the image series in Figure 1c shows that the dendrite growth is not unidirectional, even on macroscopic length scales, but instead twists before growing to short circuit the cell in the final image frame. There have been reports that microstructure growth could occur at the base of existing dendrites (14). This process can clearly be ruled out because once the growth zones move past a given region, the observed microstructure does not change for the remainder of the experiment. This effect is observed

when comparing, for example, the third to fourth images in Figure 1c (and the associated time steps in the movie), where new growth is observed on both the left- and right-hand sides of the cell during the same time period.

Understanding the source of the observed image contrast around the dendrites is important if the methodology is to be fully exploited. The microstructures are expected to be very small, of the order of 1-3 μm in diameter (5, 14, 15), making it unlikely that the 80% drop in signal intensity of the 180 x 180 x 180 μm image voxels can be due solely to the local displacement of the electrolyte by the dendrites. Furthermore, local displacement effects would not result in any attenuation of the total image intensity, yet it decreases approximately linearly during charging (Figure 2) and by a total of ca. 18% by the end of charging. Assuming that the concentration of the protonated species in the electrolyte is uniform, the signal changes can be correlated to a change in the observed electrolyte volume (right-hand axis in Figure 2). This conversion allows for a direct comparison with the volume of Li microstructure that grows if all of the deposited lithium grows as microstructure (dashed line in Figure 2). Under these assumptions, the microstructure occupies 2.03 mm^3 by the end of charging, while the signal lost in the images corresponds to a lost volume of over 40 mm^3. This 20-fold difference between the expected microstructure volume and the affected region of the proton signal can be explained on the basis of susceptibility effects and rf inhomogeneities close to the conducting microstructure.

These mechanisms can be quantified through B_0 and B_1 field calculations. A section of the reconstructed dendrite from the MRI results is chosen as a model system on which to perform these calculations, as described in the Methods section. Dendrites can be thought of as fractal (16) and hence this macroscopic shape is expected to be representative of the dendrite shape on the microscopic scale. The chosen structure resembles sections of lithium microstructures seen in SEM (15) and X-Ray phase contrast imaging (17).

Lithium metal is strongly paramagnetic (volume susceptibility, $\chi_{\mathrm{Li}} = 24.1 \times 10^{-6}$) (18), thus a strong local field is induced in the direction of an applied B_0 field, leading to changes in the observed frequencies of the nuclear species in the electrolyte around the object. The modification to B_0 is calculated using a FFT method (12, 19, 20), that operates on a Cartesian grid of susceptibility values representing the Li dendrite used for the B_1 field calculations. Figure 3 displays orthogonal cross sections of the B_0 field map obtained from the susceptibility calculations and a histogram showing the variation in the B_0 field across the full voxel. A significant perturbation of 10-15 ppm is observed in the B_0 field close to the dendrite, matching

well with ^{7}Li MRI (7, 10) and NMR (6, 8, 21) results, where dendrites are observed to shift by up to 15 ppm relative to the bulk metal resonance. The effects are long-ranged, impacting the local field for all of the positions inside the voxel, albeit by small amounts. For example, the field around a spherical object falls off with $1/r^3$, and around a cylindrical object with $1/r^2$. The histogram combining all the positions inside the voxel (Figure 3a), plotted on a logarithmic scale, shows that 91.9% of the locations experience a field perturbed by less than 2 ppm. We note that these effects can result in minor mis-registration of some of the detected signals in the frequency-encoded dimension (96 points were acquired in the read or directly-observed dimension with a spectral width of 80 kHz so a frequency shift of ca. 2 ppm will result in signal mis-registration by 1 voxel). This effect results in minor additional image contrast and could be reduced using an increased spectral width for the acquisition.

The calculated B_1^+ field distribution is shown for two orthogonal planes in Figure 4, including the absolute magnitude of the field (Figure 4b,c) and its phase (Figure 4e,f), as well as histograms showing the distribution of each quantity over all of the electrolyte sites in the voxel (Figure 4a,d). The lithium dendrite is modeled as a perfect conductor. The rf field, expected to be homogenous in the absence of the dendrite, has changed to a highly anisotropic distribution, For the most part, the magnitude of the field is increased in the *x*-*z* plane and reduced in the *y*-*z* plane. According to the boundary conditions the B_1^+ field perpendicular to a metal surface is significantly attenuated, as also demonstrated in previous calculations and MRI experiments (12). The maximum deviations from the unperturbed magnetic field occur close to the surface of the metal, in electrolyte regions that are less than 5 μm away from the metal surface. There are also strong changes in the phase of the field close to the dendrite structure (Figure 4e,f). However, the analysis of the rf field distribution over the whole voxel (Figure 4a,c) shows that it is not significantly perturbed for the majority of the electrolyte locations in the voxel (93.9% are within 20% of the unperturbed field amplitude, and 91.2% within $\pi/20$ radians of its phase). The histograms also show there to be an approximately equal distribution of sites in the voxel where an increase in the field intensity/phase is observed versus a decrease. Both the amplitude and the phase changes in B_1^+ impact the excited and detected signal for this voxel in the MRI experiment.

The B_0 and B_1^+ field maps in Figures 3 and 4 are used to calculate the detected signal intensity of the dendrite-occupied voxel in a gradient-echo (T_2*-weighted) MRI experiment. Spin echo MRI experiments could also be used but the inhomogeneities in the rf field would compromise the use of fast/turbo spin echo sequences, wherein the acquisition of consecutive lines of *k*-

space with (imperfect) refocusing π-pulses under a single excitation would lead to image distortions. Slower experiments would therefore be required, and would not be amenable to *in situ* studies.

In the vector model used to describe the dynamics of the bulk MR magnetization vector, the spatial variation of B_1^+ impacts the NMR signal excited by an rf pulse according to

$$M_j^+ = -i\sin(\alpha_j)\frac{B_{1,j}^+}{\left|B_{1,j}^+\right|}M_{0z}^j, \qquad [1]$$

where M_{0z}^i is the equilibrium z magnetization at the j^{th} position in the voxel and α_j is the flip angle defined as $\alpha_j = \gamma\left|B_{1,j}^+\right|\tau_{\text{p}}$, with γ the gyromagnetic ratio of the nucleus and τ_{p} the pulse duration. From Eq. (1) it is clear that changes in the phase of B_1^+ are manifested in the phase of M^+.

In steady-state imaging experiments such as FLASH, low flip angles and repetition times (TR) are used to reduce experiment times, partially saturating the equilibrium z magnetization until an equilibrium value M_{0z} is reached. The spatial variation in α leads to a spatial variation in the equilibrium z-magnetization that must also be accounted for, and is given by

$$\frac{M_{0z}^j}{M_0} = \frac{1-\exp\left(-\frac{\text{TR}}{T_1}\right)}{1-\cos(\alpha_j)\exp\left(-\frac{\text{TR}}{T_1}\right)}, \qquad [2]$$

where M_0 is the length of the fully relaxed magnetization vector, TR is the repetition time used in the experiment, and T_1 the spin-lattice relaxation of the nuclear spin, which is assumed to be constant ($T_1 = 2s$) within the voxel.

According to the principle of reciprocity (22), the local variation in the phase and amplitude of the B_1 field also impacts the detected signal,

$$S_j = 2\omega M_j^+ B_{1,j}^{(-)*}, \qquad [3]$$

where S_j is complex and represents the signal amplitude and phase, and ω is the Larmor frequency. All of the signals from each position inside the voxel, S_j, are summed to give the overall intensity, S_{voxel} that is predicted for the single voxel in the image. Depending on the type of imaging experiment used, further weighting of the signal intensity is expected (i.e. by T_1, T_2 or

T_2^*). Gradient echo (GE) sequences such as FLASH are T_2^*-weighted and are sensitive to these types of B_0 inhomogeneities within the voxel. The detected signal intensity is consequently modified to

$$S_{voxel}^{GE} = \sum_j S_j \, exp\left(i\omega_j^{off} \cdot TE\right), \qquad [4]$$

where $\omega_j^{\mathrm{off}} = 2\pi\nu B_{0,\mathrm{eff}}^{j}/10^6$, is the angular frequency offset in the rotating frame for the j^{th} location in the voxel (from the susceptibility calculations) and $\mathrm{TE} = 2\ \mathrm{ms}$, the echo time used in the experiment. The signals are normalized by S_{voxel}^{0}, the expected signal intensity for the voxel when no dendrite is present (i.e. no scattered rf field, $H_1^{\mathrm{scat}} = 0$, and $\mathrm{TE} = 0$, $\omega^{\mathrm{off}} = 0$ and $M_{0z} = M_0$). All experimental parameters used in the calculation correspond to the values from the FLASH experiments used to acquire the images from Figure 1.

Maps of the signal intensity, $\left|S_j^{\mathrm{GE}}\right|$ (Figure 5b,c) follow the trends shown in the B_1^+ field maps (Figure 4b,c). This is seen because the FLASH experiment uses a low flip angle pulse and in the regime where TR is sufficient to avoid saturation of M_{0z}^{j} then $\left|S_j^{\mathrm{GE}}\right|$ is proportional to the amplitude of B_1^+. Maps of the signal phase, $\Phi(S_j^{\mathrm{GE}}) = \tan^{-1}\left[\mathrm{Re}(S_j^{\mathrm{GE}})/\mathrm{Im}(S_j^{\mathrm{GE}})\right]$, (Figure 5e,f) show there to be significant changes over relatively short distances in the voxel, with particularly strong fluctuations close to the dendrite. These effects are predominantly due to the changing B_0 field throughout the volume and the resulting differences in the relative phase that is accumulated during the echo time in the experiment, although the changing B_1^+ phase will also play a role. The changes in the signal phase have a profound effect on the total signal intensity of the voxel because of partial signal cancellations, resulting in significant attenuation of the detected signal.

The voxel considered in Figures 3-5 has a volume of 100 μm^3 with ca. 3.5% of the total volume occupied by dendritic lithium metal. To understand the dominant effects that contribute to the signal intensity under different growth conditions, voxels of different sizes were also considered, containing the same dendrite structure, but enlarging the surrounding region. The sum of the signal intensities is shown in Figure 6a, where the individual contributions from the susceptibility and B_1^+ field effects are also considered. It is seen that the B_1^+ inhomogeneities lead to almost no change in the detected signal. This effect can be attributed to the fact that B_1^+ increases in some regions around the voxel while decreasing in others. Meanwhile, the susceptibility effects

can explain almost all of the complete signal attenuation when only a modest fraction of the cell is occupied by dendrites (60 μm^3 voxel, 15% occupied by dendrite). In the MRI experiment results, a threshold of 20% of the maximum signal amplitude of a given voxel ($I_{\mathrm{threshold}} = 0.2I_{\mathrm{max}}$) is used to designate locations where dendrites are growing. In Figure 6a this condition is satisfied for the 80 μm^3 voxel with 7% of its volume occupied by the dendrite. This observation confirms that high levels of contrast are possible without individual voxels containing a significant volume of metal displacing the electrolyte.

The results in Figure 6a relate the dendrite volume in a single voxel to the MRI signal intensity of that voxel, and can be extrapolated to cover the full signal range (dashed black lines in Figure 6a). This relationship can then be used to convert the experimental MRI signal intensities of each voxel, $S_{\mathrm{voxel}}(t)/S_{\mathrm{voxel}}(t=0)$, into estimates of the local dendrite volume and therefore the overall volume of dendrites that have grown inside the battery (Figure 6b, methodology described in more detail in the Supporting Information). The results are close to the calculated theoretical volume (dashed line in Figure 6b, calculation described in the caption of Figure 2). The total dendrite volume is predicted to be 2.7 mm^3 whereas 2.0 mm^3 is expected if all of the deposited lithium forms dendrites with the same density as bulk lithium metal. Additional calculations performed on highly symmetric (spherical and cylindrical) and random lithium geometries (detailed in the Supporting Information) produce lower estimates of the total grown dendrite volume (1.6 mm^3 for the sphere and random morphologies, and 2.2 mm^3 for a rotationally-averaged cylinder). The model dendrite geometry does therefore help in examining the influence of morphology on the quantification. On the other hand, the relatively small range of the estimates, which fall within approximately 80-135% of the theoretical dendrite volume, suggest that the role of morphology is minor and while there is some uncertainty in the quantification of the dendrite volume, there is currently no alternative methodology that would allow one to perform such an assessment *in situ*. Indeed, the agreement between the current experiment and theory is quite surprising, considering that a naïve analysis simply based on signal intensities would overestimate the dendrite volume by a factor of 20 (Figure 2). This analysis therefore shows that B_1 and especially B_0 effects allow a nearly accurate explanation of the experimentally observed signal attenuation.

In summary, we present here methodology for the non-invasive assessment of Li-ion battery cells, where the growth of microstructure and dendrites is monitored indirectly via ^{1}H MRI in 3D at different charging states. One of the main advantages of the method is a dramatic increase in sensitivity, since direct observation of low sensitivity nuclei such as ^{7}Li is not required, thus

enabling wide-ranging applications to different battery chemistries (e.g. sodium), including the use of electrodes with insensitive or inactive NMR nuclei. Furthermore, the speed afforded by this ^{1}H method offers a significant advantage over current approaches, which will be an important factor for the study of different cycling behaviors. The approach provides a 'one nucleus fits all' solution for studying a broad range of different battery models (for example Li, Na, and Mg cells) under the same conditions, with no special hardware demands. Significant image contrast amplification (up to a factor 20) is demonstrated to arise from the local B_0 inhomogeneities originating from the susceptibility differences. These techniques could be used for testing dendrite growth models and the effectiveness of dendrite-suppressing approaches such as pulsed charging (23, 24) or the use of advanced electrode, electrolyte or separator materials.

Materials and Methods

Sample Preparation. A schematic of the electrochemical cell used is shown in Figure 7a. It consists of two 6.35 mm diameter, circular lithium metal (Sigma Aldrich) electrodes, separated by an 8 mm electrolyte region filled with 1M $LiPF_6$ in 1:1 by volume ethylene carbonate (EC): dimethyl carbonate (DMC) electrolyte (Novolyte) mixed with 5 % poly(methyl methacrylate) (PMMA). Copper mesh current collectors were pressed into the lithium metal electrodes and attached to stranded copper wire that connected them to the external circuit. The cell was prepared in an argon glove box (O_2 and H_2O < 0.2 ppm). Electrochemical cycling was performed using a Biologic VSP potentiostat, with the current applied in the direction from the bottom electrode (positive electrode) to the top electrode (negative electrode). Dendrite growth was initiated prior to the collection of the *in situ* ^{1}H images by charging the cell at 50 μA (0.16 mA cm^{-2}) for 72 hours. During the MRI experiments the cell was charged at 160 μA (0.51 mA cm^{-2}) for a total of 26.1 hours.

Magnetic Resonance Imaging. The MRI experiments were performed on a Bruker Ultrashield 9.4 T Avance I spectrometer containing a Bruker Micro2.5 gradient assembly and operating at 400.1 MHz for ^{1}H. A Bruker Micro2.5 imaging probe was used to collect all of the data, with a Bruker WB40 25 mm i.d. coil insert for ^{1}H experiments. The cell was aligned in the magnet such that B_0 (and the *z* axis of the gradients) was aligned perpendicular to the face of the electrodes (as illustrated in Figure 7a). The cells were centered in the coil, the excitation profile of which was found to be approximately 15 mm, thus ensuring uniform excitation over all of the

components in the cell. 3D 1H MRI experiments were performed using the 3D FLASH sequence implemented in Paravision 5.1, using an echo time (TE) of 2 ms, repetition time (TR) of 100 ms, nominal flip angle (α) of 10°, and 4 scans for signal averaging. The field of view (FOV) was 11.52 x 11.52 x 17.28 mm in the *x*,*y*, and *z* direction respectively, with a *k*-space consisting of 64 phase encoded points in the *x* and *y* directions and 96 points in the readout direction along *z*. Only the central 50 *k*-space points in the phase directions were acquired in order to accelerate the acquisition. This resulted in a 3D image covering both electrodes and the electrolyte region in the cell with an isotropic resolution of 180 μm, with a total experiment time of 16 mins 40 s.

Radiofrequency Field Calculations. The interaction between a microscopic conducting object and an applied radiofrequency field was simulated using finite element calculations to solve Maxwell's equations in 3D. The calculation was performed within the COMSOL simulation suite (25). A 3D geometry representing a lithium dendrite structure was constructed from a section of the FLASH MRI data. The raw voxel data was first converted to an STL format using the vtk Python module (26). The STL mesh was then imported into Blender, where a cuboid base representing the electrode surface was added and the surface closed. Minor meshing errors in the resulting structure were fixed using Gmsh (27) before the object, displayed in Figure 7b, was imported into COMSOL. The dendrite was placed at the center of a 280 μm radius sphere, filled with electrolyte surrounding the dendrite. Compared to the dendrite electrical conductivity of 3.774 x 10^7 $\Omega^{-1}\mathrm{m}^{-1}$, the conductivity of the electrolyte region was approximated as zero, The finite element mesh consisted of 67400 tetrahedral and 5942 triangular elements, covering the surface of the dendrite and spherical boundary, and volume between the two. Dirichlet boundary conditions were used on the surface of the sphere to specify the incoming field, $H_1^{\mathrm{in}} = (0,1,0)$, while perfect conductor boundary conditions were used on the surface of the dendrite. When using calculations with finite conductivity, the magnitude of an object's conductivity has a negligible effect on B_1 distortions (12, 28). The computations were performed in the rotating frame at a frequency of 400 MHz (the Larmor frequency of ^{1}H in the MRI experiments) using the BiCGStab solver. The calculation took approximately 1 hour running on a desktop computer with 32GB RAM and an Intel i7 processor with 6 cores. Only the x and y components of the calculated field are included in the MR signal calculations as the components perpendicular to the direction of the external magnetic field, $B_{1x,y} = \mu_0(H_{1x,y}^{\mathrm{in}} + H_{1x,y}^{\mathrm{scat}})/H_{1x,y}^{\mathrm{in}}$, where $H_{1x,y}^{\mathrm{scat}}$ are the x and y components of the scattered field and the values are normalized according to the incoming field. These quantities were extrapolated onto a 200×200×200 grid covering a 200 μm^3 region centered on the dendrite, and exported to Python for further analysis. The

exported fields are used to calculate the rf fields in the positively and negatively rotating frames (22, 29),

$$B_{1,j}^{+} = B_{1x}^{j} + iB_{1y}^{j} \quad [5]$$

$$B_{1,j}^{-} = B_{1x}^{j} - iB_{1y}^{j} \quad [6]$$

as these are the fields that interact with the nuclear spin magnetization in the rotating frame, where the B_{1x}^{j} and B_{1y}^{j} are complex quantities.

Susceptibility Calculations. The susceptibility-induced modification to B_0 caused by the paramagnetic lithium metal structure inside the voxel was calculated this using a FFT method that has been described elsewhere (19, 20). A regular 3D grid of volume susceptibility values is taken as the calculation input, which was constructed directly from the gridded COMSOL output, with $\chi = \chi_{\mathrm{Li}}$ (where $\chi_{\mathrm{Li}} = 24.1 \times 10^{-6}$) (18) for grid points inside the dendrite and $\chi = 0$ elsewhere, roughly approximating the electrolyte susceptibility. This 250^3 cell was padded with zeros to make a 512^3 cell on which the calculations were performed. The output from the calculations is the susceptibility-induced offset to the B_0 field at each of the j points in the grid, $B_{0,\mathrm{eff}}^{j}$, in units of ppm.

Acknowledgements

The NMR/MRI methodology as well as rf and static field calculations were supported by the US National Science Foundation, under grant no. CHE 1412064. The electrochemistry and battery components of the work were supported as part of the NorthEast Center for Chemical Energy Storage (NECCES), an Energy Frontier Research Center funded by the U.S. Department of Energy (DOE), Office of Science, Basic Energy Sciences, under Awards DE-SC0001294 and DE-SC0012583 (in situ methodology), including NECCES matching funds from the New York State Energy Research Development Authority (NYSERDA) (H.J.C.), by the Assistant Secretary for Energy Efficiency and Renewable Energy, Office of FreedomCAR and Vehicle Technologies of the U.S. DOE under Contract DE-AC02-05CH11231, under the Batteries for Advanced Transportation Technologies (BATT) Program subcontract #7057154.

References

1. Tarascon J-M, Armand M (2001) Issues and challenges facing rechargeable lithium batteries. *Nature* 414(6861):359–367.

2. L. Sannier RB (2005) Room temperature lithium metal batteries based on a new Gel Polymer Electrolyte membrane. *J Power Sources* 144(1):231–237.

3. Crowther O, West AC (2008) Effect of Electrolyte Composition on Lithium Dendrite Growth. *J Electrochem Soc* 155(11):A806–A811.

4. Brissot C, Rosso M, Chazalviel J-N, Baudry P, Lascaud S (1998) In situ study of dendritic growth inlithium/PEO-salt/lithium cells. *Electrochimica Acta* 43(10–11):1569–1574.

5. Orsini F, et al. (1998) In situ Scanning Electron Microscopy (SEM) observation of interfaces within plastic lithium batteries. *J Power Sources* 76(1):19–29.

6. Bhattacharyya R, et al. (2010) In situ NMR observation of the formation of metallic lithium microstructures in lithium batteries. *Nat Mater* 9(6):504–510.

7. Chang HJ, et al. (2015) Correlating Microstructural Lithium Metal Growth with Electrolyte Salt Depletion in Lithium Batteries Using 7Li MRI. *J Am Chem Soc* 137(48):15209–15216.

8. Chang HJ, et al. (2015) Investigating Li Microstructure Formation on Li Anodes for Lithium Batteries by in Situ 6Li/7Li NMR and SEM. *J Phys Chem C*. doi:10.1021/acs.jpcc.5b03396.

9. Hu JZ, et al. (2016) In situ 7Li and 133Cs nuclear magnetic resonance investigations on the role of Cs+ additive in lithium-metal deposition process. *J Power Sources* 304:51–59.

10. Chandrashekar S, et al. (2012) 7Li MRI of Li batteries reveals location of microstructural lithium. *Nat Mater* 11(4):311–315.

11. Salager E, et al. (2014) Solid-State NMR on the family of positive electrode materials Li2Ru1-ySnyO3 for Li-ion batteries. *Chem Mater*. doi:10.1021/cm503280s.

12. Ilott AJ, et al. (2014) Visualizing skin effects in conductors with MRI: Li MRI experiments and calculations. *J Magn Reson* 245:143–149.

13. Romanenko K, Forsyth M, O'Dell LA (2014) New opportunities for quantitative and time efficient 3D MRI of liquid and solid electrochemical cell components: Sectoral Fast Spin Echo and SPRITE. *J Magn Reson* 248:96–104.

14. Yamaki J, et al. (1998) A consideration of the morphology of electrochemically deposited lithium in an organic electrolyte. *J Power Sources* 74(2):219–227.

15. López CM, Vaughey JT, Dees DW (2009) Morphological Transitions on Lithium Metal Anodes. *J Electrochem Soc* 156(9):A726–A729.

16. Fleury V (1997) Branched fractal patterns in non-equilibrium electrochemical deposition from oscillatory nucleation and growth. *Nature* 390(6656):145–148.

17. Eastwood DS, et al. (2014) Three-dimensional characterization of electrodeposited lithium microstructures using synchrotron X-ray phase contrast imaging. *Chem Commun* 51(2):266–268.

18. Gugan D (1997) Martensitic transformation of lithium: Magnetic susceptibility measurements. *Phys Rev B* 56(13):7759.

19. Salomir R, de Senneville BD, Moonen CT (2003) A fast calculation method for magnetic field inhomogeneity due to an arbitrary distribution of bulk susceptibility. *Concepts Magn Reson* 19B(1):26–34.

20. Marques JP, Bowtell R (2005) Application of a Fourier-based method for rapid calculation of field inhomogeneity due to spatial variation of magnetic susceptibility. *Concepts Magn Reson Part B Magn Reson Eng* 25B(1):65–78.

21. Trease NM, Zhou L, Chang HJ, Zhu BY, Grey CP (2012) In situ NMR of lithium ion batteries: Bulk susceptibility effects and practical considerations. *Solid State Nucl Magn Reson* 42:62–70.

22. Hoult DI (2000) The principle of reciprocity in signal strength calculations—A mathematical guide. *Concepts Magn Reson* 12(4):173–187.

23. Mayers MZ, Kaminski JW, Miller TF (2012) Suppression of Dendrite Formation via Pulse Charging in Rechargeable Lithium Metal Batteries. *J Phys Chem C* 116(50):26214–26221.

24. Aryanfar A, et al. (2014) Dynamics of Lithium Dendrite Growth and Inhibition: Pulse Charging Experiments and Monte Carlo Calculations. *J Phys Chem Lett* 5(10):1721–1726.

25. COMSOL Multiphysics (COMSOL AB, Stockholm, Sweden.) Available at: www.comsol.com.

26. Schroeder, Will; Martin, Ken; Lorensen, Bill (2006) *The Visualization Toolkit* (Kitware). 4th Ed.

27. Geuzaine C, Remacle J-F (2009) Gmsh: A 3-D finite element mesh generator with built-in pre- and post-processing facilities. *Int J Numer Methods Eng* 79(11):1309–1331.

28. Vashaee S, Goora F, Britton MM, Newling B, Balcom BJ (2015) Mapping B1-induced eddy current effects near metallic structures in MR images: A comparison of simulation and experiment. *J Magn Reson* 250:17–24.

29. Collins CM, Smith MB (2001) Calculations of B(1) distribution, SNR, and SAR for a surface coil adjacent to an anatomically-accurate human body model. *Magn Reson Med* 45(4):692–699.

Figures

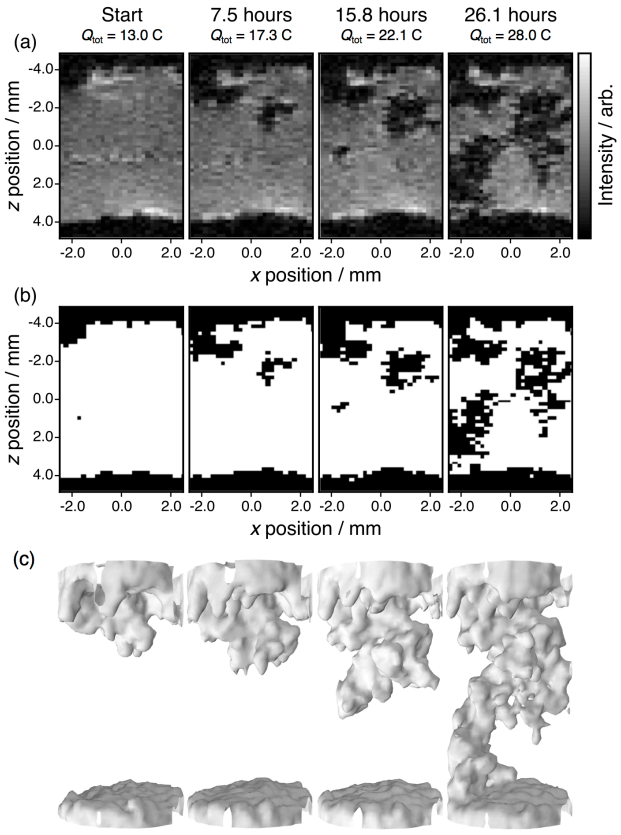

Figure 1. *In situ* ^{1}H 3D FLASH imaging results from the electrochemical cell, with each 3D image acquired in 16 mins 40 s. The cell was charged at 50 μA (0.16 mA cm^{-2}) for 72 hours prior to these measurements, and then charged at 160 μA (0.51 mA cm^{-2}) for the times specified, with the total charge applied also given in Coulombs. (a) 2D slices from four time points, (b) segmented images of the results from (a) where $I_{\mathrm{threshold}} = 0.2I_{\mathrm{max}}$, (c) 3D segmented images of the same time points with an additional Gaussian filter applied to smoothen the visualization.

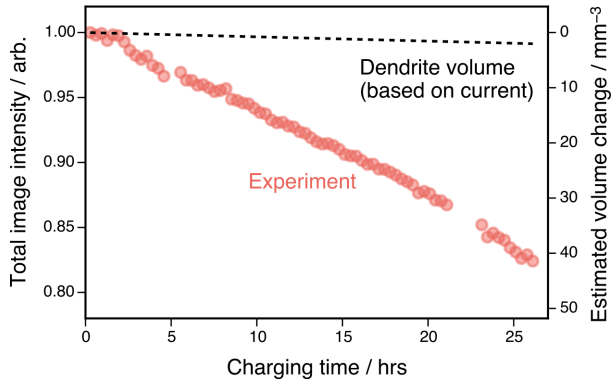

Figure 2: Trends in the total MRI image intensity correlated with microstructure volume. The image intensity is converted to volume by assuming volume ∝ signal intensity (i.e. concentration is uniform) and then normalizing by the starting volume of the electrolyte as estimated from the image at $t = 0$ (236 mm^3). The dendrite volume is estimated by converting the total charge transferred, $Q = It$ (current times time) to the number of moles of lithium, $n_{\mathrm{Li}} = Q/F$ where F is the Faraday constant, and then to a volume, $V_{\mathrm{Li}} = n_{\mathrm{Li}}\mathrm{Mr}_{\mathrm{Li}}/\rho_{\mathrm{Li}}$ using the density of lithium metal, $\rho_{\mathrm{Li}} = 0.534\ \mathrm{g\ cm^{-3}}$. Numerical errors associated with the experimental image intensity are within the marker size.

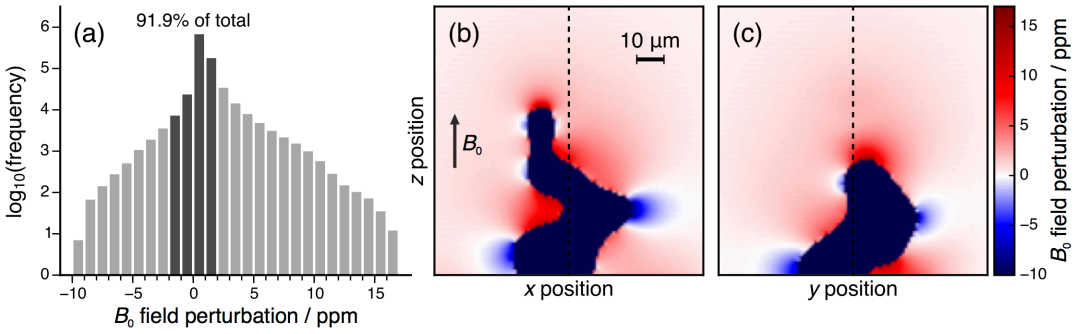

Figure 3: Results from the susceptibility calculations. (a) Histogram of the B_0 field perturbations at every position in the 3D voxel. (b,c) B_0 field maps at orthogonal slices through the simulation voxel. $\boldsymbol{B_0}$ is aligned along z as indicated in (b), dotted lines on (b) and (c) show the slice positions.

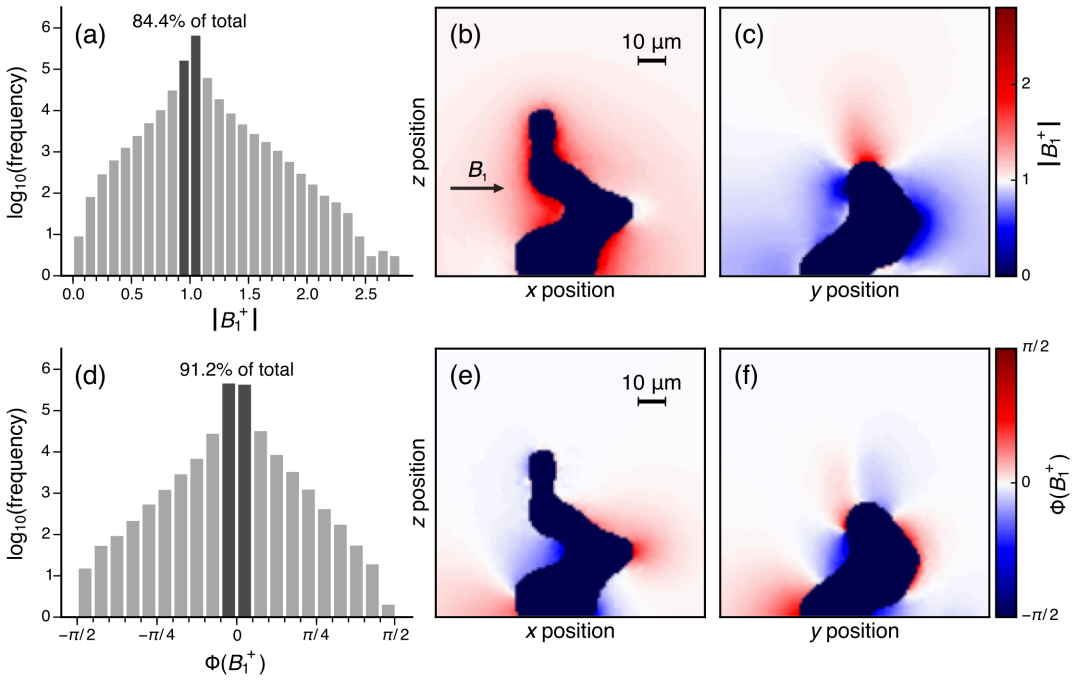

Figure 4: Results from the rf field intensity and phase calculations. (a,d) Log-scale histograms for the amplitude and phase of B_1^+ across the whole voxel. (b,c,e,f) Maps of the amplitude (b,c) and phase (e,f) of B_1^+ in two orthogonal slices through the voxel. B_1^+ propagates in the x direction as indicated in (b).

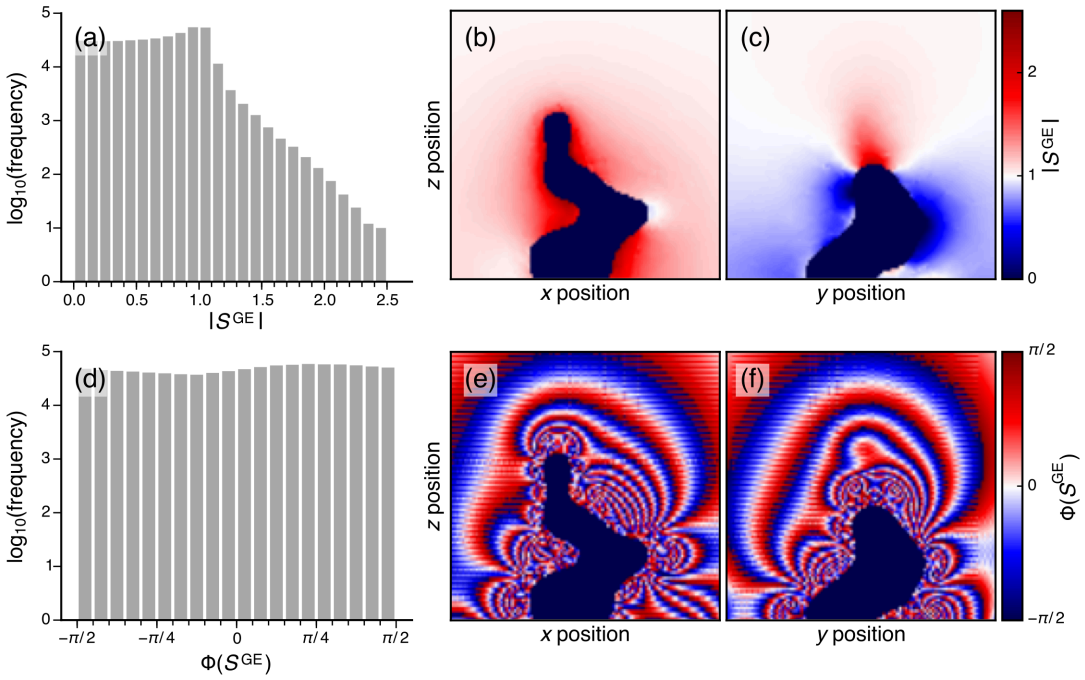

Figure 5: Results from the signal intensity and phase calculations. (a,d) Log-scale histograms for the amplitude and phase of the detected signal across the whole voxel. (b,c,e,f) Maps of the amplitude (b,c) and phase (e,f) of the detected signal in two orthogonal slices through the voxel.

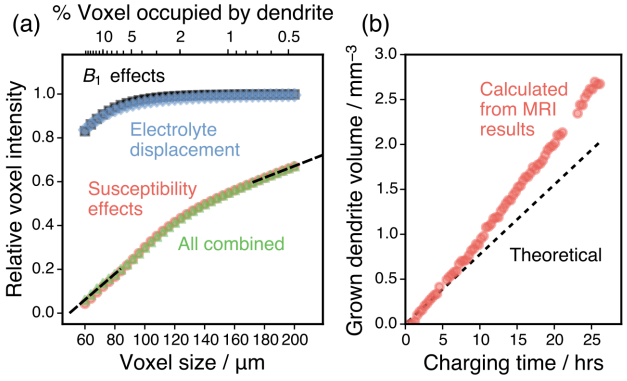

Figure 6: Analysis of calculated voxel size effects. (a) Calculated signal attenuations for differently sized voxels, given relative to the maximum signal for each cell size. Contributions of different sources of signal attenuation are calculated separately (for B_1 alone $\omega_j^{\text{off}} = 0$ and for susceptibility alone $B_{1,j}^{+} = B_{1,\text{incoming}}^{+}$ for all j, with both conditions used to isolate displacement effects). Black dashed lines illustrate the linear extrapolation of the combined results. (b)

Comparison between the calculated and theoretical dendrite volume in the battery throughout the experimental time series. Numerical errors associated with the calculated dendrite volume are within the marker size.

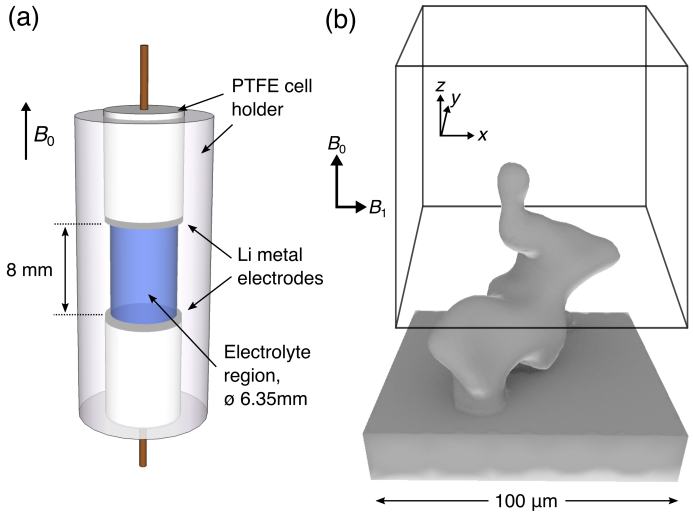

Figure 7: Schematics of (a) the electrochemical cell and (b) the model dendrite used for the calculations, with the box drawn to illustrate a given MRI voxel position around the dendrite.